Towards an optical clock for space: Compact, high-performance optical lattice clock based on bosonic atoms

S. Origlia, M. S. Pramod, and S. Schiller

Institut für Experimentalphysik, Heinrich-Heine-Universität Düsseldorf, 40225 Düsseldorf, Germany

Y. Singh and K. Bongs

University of Birmingham, Birmingham B15 2TT, United Kingdom

R. Schwarz, A. Al-Masoudi, S. Dörscher, S. Herbers, S. Häfner, U. Sterr, and Ch. Lisdat

Physikalisch-Technische Bundesanstalt, 38116 Braunschweig, Germany

Optical clocks operated on satellites are expected to open up new opportunities in time transfer, geodesy, fundamental physics, and satellite navigation. Here we demonstrate an important first step towards this goal: a modular, compact, optical lattice clock (OLC) system that achieves 2.0×10^{-17} fractional uncertainty. The clock is operated with bosonic strontium and improves the performance of bosonic OLCs by a factor of 30. This has important implications for future use of bosonic OLCs in fundamental physics and metrology. We make use of the clock's metrological performance to measure, with independent clocks, the isotope shift of the $^1S_0 \rightarrow {}^3P_0$ transitions of ^{88}Sr and ^{87}Sr, with an uncertainty of 12 mHz. The ratio of the transition frequencies is thus determined with 3×10^{-17} fractional uncertainty.

I. INTRODUCTION

Optical clocks, in particular optical lattice clocks (OLCs) [1], have made strong progress in the past decade, in terms of both accuracy and stability [2–4]. This progress continues at a remarkable pace [5,6]. Clocks operated in different metrological institutes have been compared, in part employing long-distance optical links [7–10], permitting the measurement of the frequency ratios of various clocks [8,11–15] and tests of local Lorentz invariance [16,17]. Improved limits to a hypothetical present-day time variation of certain fundamental constants have also been set [18–20]. The most accurate clock comparisons have achieved a fractional uncertainty in the 1.4×10^{-18} range [6] and may be regarded as the most precise in any field of physics. The feasibility of using OLCs for the realization of timescales has also been demonstrated [21–23].

Recently, a strontium OLC [24] operated in a car trailer has been employed in measurement campaigns [15], showing the prospects of a transportable reference optical clock and of clock-based geodesy. Another application coming into focus is the use of clocks for the detection of particles beyond the standard model. One approach consists of precisely measuring the isotope shift of optical transitions of several isotopes [25]. A first step in this direction was reported in Ref. [26]. Another visonary approach is a world-spanning observatory for topological dark matter [27].

A far-reaching goal is the operation of optical clocks in space. This is a logical step to be taken after completing the upcoming clock missions based on *microwave* cold-atom clocks, foreseen both for the future Chinese space station [28] and for the International Space Station (ISS) [29,30]. These space missions are conceived as demonstration and

science missions for worldwide time and frequency dissemination, worldwide clock geodesy, and establishment of a world-spanning clock network for fundamental physics tests, including the search for dark matter [27]. The microwave clocks built for space applications are designed to reach an instability and inaccuracy similar to that of the best ground-based cold Cs clocks, 2×10^{-16}. An *optical* clock with a tenfold better performance, for instance, will allow a corresponding performance enhancement of the listed applications. In particular, clock-based geodesy will then become competitive with "conventional" satellite-based geodesy in terms of geopotential resolution. The spaceborne optical clock could also support the above-mentioned dark matter observatory.

Within an international consortium we have conceived a space mission on the ISS (I-SOC) based on high-performance time/frequency links and an OLC (chosen for the high frequency stability achievable with this clock type) [31,32]. We have developed an OLC demonstrator model [33,34] (Fig. 1), intended to demonstrate the feasibility of a clock with instability and inaccuracy both at the low-10^{-17} level *and* of compact dimensions. The improved performance compared to the ACES goals ($100\times$ for instability, $10\times$ for inaccuracy), will enable comparison of ground clocks at the 1×10^{-18} level via the space clock, and improve tenfold (to 2×10^{-7} level) a measurement of the gravitational time dilation caused by the earth. Compactness is imposed by the constraints for an external payload attached to the ISS Columbus module of the European Space Agency.

In this paper, we present the detailed metrological characterization of the atomics and laser packages of the demonstrator model, performed with a stationary laboratory clock
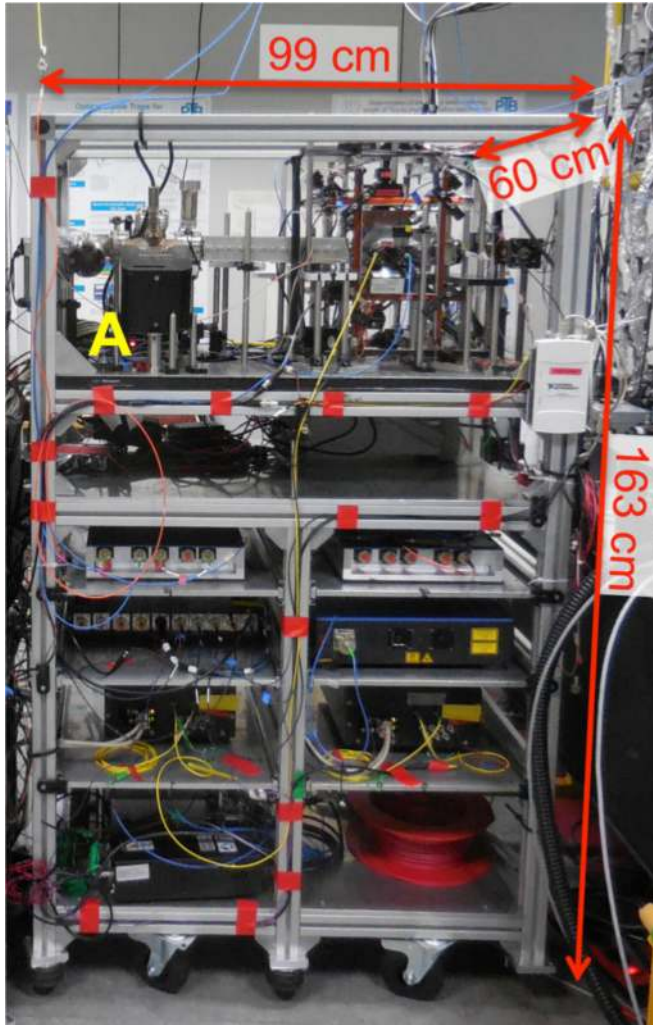
FIG. 1. The OLC rack including the atomics package (A) and the laser breadboards below. The clock laser is not included.

FIG. 2. CAD drawing of the compact atomics package.

laser. We employed bosonic ^{88}Sr atoms and achieved the best performance of any bosonic OLC so far, with an inaccuracy of 2×10^{-17} relative to the transition frequency. This represents an improvement by a factor of 30 compared with previous works on bosons [26] and allowed us to perform an isotope shift measurement at the 3×10^{-17} level relative to the transition frequency. The potential of bosonic OLCs with performance beyond the Cs cold-atom clock had been foreseen a long time ago [35]; this is the first experimental demonstration.

II. THE DEMONSTRATION MODEL

The demonstrator model is shown in Fig. 1. It consists of a compact atomics package (Fig. 2) [33], a set of compact cooling and manipulation lasers, a compact and robust frequency stabilization system for the lasers [36], and a robust and transportable clock laser reference cavity, whose performance is described elsewhere [37]. The volume envelope is 1 m^3, excluding electronics. The total mass is moderate, <250 kg, excluding electronics. The atomics package (Fig. 2) is also compact. The vacuum chamber for atom trapping is
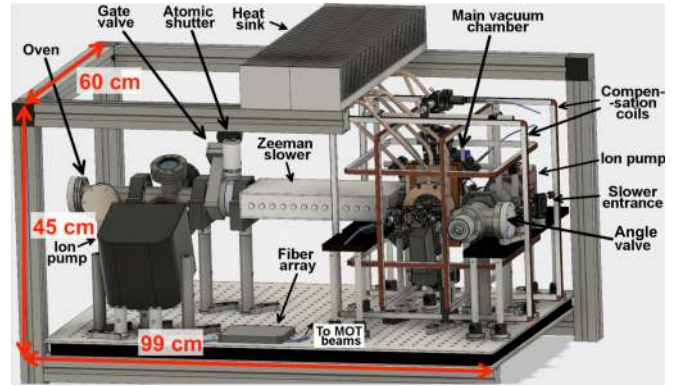
particularly small (outer size $50 \times 50 \times 20$ mm^3). To reduce the power consumption, we integrated a high-efficiency atomic oven [38], a permanent magnet Zeeman slower [39], a compact science chamber, and a compact MOT coils assembly [33]. The latter requires moderate current and dissipates 8 W on average. These aspects are also crucial for a space OLC.

III. LATTICE CLOCKS WITH BOSONS

Bosonic OLCs exhibit some disadvantages compared with fermionic OLCs, which have impeded their use for metrological applications: (i) the presence of *s*-wave collisions [40], suppressed in the case of spin-polarized fermions, and causing a significant frequency shift if uncontrolled, and (ii) a transition between the $^1S_0$ and the $^3P_0$ clock states, which is strictly forbidden as single-photon excitation and requires the application of one or more additional external fields to enable it [35,41]. These fields also cause a significant frequency shift [26,35,41,42].

A potential future advantage of bosonic isotopes using a magnetically induced clock transition is that the effective lifetime of the upper level can be considerably longer than in the fermionic isotopes. Then, future ultrastable lasers, whose coherence time exceeds the fermionic isotope level lifetime, could be advantageously employed [43].

Turning to the specific case of strontium, the isotopes used so far are ^{87}Sr (fermion) and ^{88}Sr (boson). The bosonic isotope is also attractive for realizing a simplified OLC, e.g., for transportation or for use in space on a satellite, where robustness and reliability are essential. Compared with ^{87}Sr, the atom cooling and clock spectroscopy are conceptually and technically simpler, thanks to the higher natural isotopic abundance (83% for ^{88}Sr versus 7% for ^{87}Sr) and absence of hyperfine structure [1,44]. Furthermore, the Stark shift cancellation wavelength ("magic" lattice wavelength) in the bosonic isotope is very weakly dependent on the direction of the external magnetic field and to the lattice polarization [2,45–47]. It is also important to develop Sr bosonic clocks further in view of the fact that isotope shifts of all bosonic Sr atoms (^{84}Sr, ^{86}Sr, ^{88}Sr, ^{90}Sr) are of interest for the search of physics beyond the standard model [25]. In this context, a highly accurate measurement of the ^{88}Sr$-^{87}$Sr isotope shift has been recently performed in a dedicated setup which allows canceling out common-mode perturbations [26].

Optical excitation of the $^1S_0 \to {}^3P_0$ clock transition in a bosonic atom can be enabled by applying a bias magnetic field B [35]. This results in a Rabi frequency $\Omega_R/2\pi = \alpha\sqrt{I}|B|$, with the clock interrogation laser intensity I and the coupling coefficient $\alpha = 198$ Hz/T$\sqrt{\text{mW/cm}^2}$ for ^{88}Sr [35]. For typical B fields, I is two to three orders of magnitude stronger compared to fermionic OLCs [35]. The interrogation light leads to a probe light shift $\Delta\nu_P = k\,I$, with $k = -18$ mHz/(mW/cm^2) [35], while the magnetic field leads to a second-order Zeeman shift $\Delta\nu_B = \beta\,B^2$, with $\beta = -23.3$ MHz/T^2 [35]. Thus, the Rabi frequency is proportional to $\sqrt{\Delta\nu_P \cdot \Delta\nu_B}$. The clock transition interrogation time, in case of Rabi spectroscopy, can be expressed as $T_\pi = \pi/\Omega_R$. Therefore, the Rabi frequency, and consequently $\Delta\nu_P$ and $\Delta\nu_B$, can be reduced using a clock laser that supports longer T_π. The two shifts and the interrogation time are related by $|\Delta\nu_P \cdot \Delta\nu_B| = 2.8\,T_\pi^{-2}$. By choosing B and I appropriately, the minimum realizable shift magnitude is $|\Delta\nu_P + \Delta\nu_B|_{\min} = 3.3/T_\pi$ (in fractional terms, 7.7×10^{-15} s$/T_\pi$). Furthermore, a long interrogation time reduces the effect of detection noise (including quantum projection noise) on the clock instability since these contributions scale as $1/\sqrt{T_\pi}$. As a consequence, operating the clock with a low atom number with moderate degradation of the stability becomes possible, which helps keep the collision shift minimal.

IV. OPTICAL CLOCK CHARACTERIZATION

A. Spectroscopy of the clock transition

In our device, atoms are cooled and trapped in a 1D, vertically oriented optical lattice (magic wavelength: $\lambda_{\text{lat}} \approx 813$ nm, $\sim$40 μm waist radius). The lattice wave polarization is linear, parallel to the magnetic field. The lifetime of the atoms in the lattice is 5 s. The clock laser (698 nm) is prestabilized to a 10-cm-long transportable cavity [48] and phase-locked to a stationary clock laser stabilized to a 48-cm-long reference cavity [49]. For most of the measurements, the stabilized laser was further phase-locked to a 1540-nm laser locked to a cryogenic silicon resonator [43], using a transfer-lock scheme [50]. The 1540-nm laser exhibits less than 10-mHz linewidth and 4×10^{-17} instability at 1 s integration time. The clock laser radiation is delivered to the atoms via a phase-noise-canceled optical fiber [51]. The clock laser waist radius is approximately 105 μm and provides a fairly homogeneous intensity profile across the atomic sample.

We investigated atom interrogation times up to $T_\pi = 8$ s, and $T_\pi = 4$ s ($\Omega_R/2\pi = 0.125$ Hz) was chosen as optimum value, the longest for which Fourier-limited clock transition linewidths were reliably observed (Fig. 3). This leads to a total cycle time of 5.3 to 6.3 s, depending on the operating conditions. The observed linewidth of 0.22 Hz is in agreement with the theoretically expected value $0.8/T_\pi \simeq 0.2$ Hz [52]. The limited contrast ($\sim$60%) can be attributed to collisional effects (see below).

Any practical combination of clock laser intensity and bias field strength matching the desired Rabi frequency and providing a shift close to $|\Delta\nu_P + \Delta\nu_B|_{\min}$ can be used. Based on the performance of the clock laser power and bias field current stabilizations, we chose a clock laser intensity
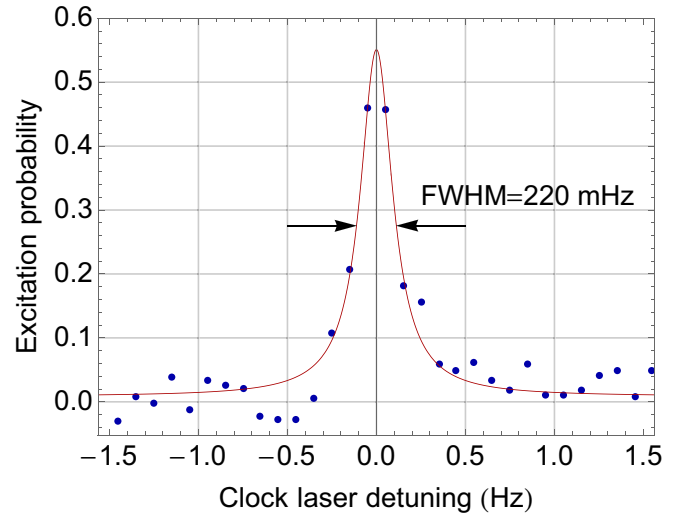

FIG. 3. Typical ^{88}Sr clock transition line for $T_\pi = 4.0$ s, bias field $B_0 \approx 0.21$ mT, clock laser intensity $I_0 \approx 28$ mW/cm^2. The line is a single scan (i.e., no averaging), with a total scan time of 165 s. The fit is a Lorentzian function.

$I_0 \approx 28$ mW/cm^2 and a bias field $B_0 \approx 0.21$ mT, leading to fractional shifts in the low 10^{-15} range.

B. Stability of systematic shifts

To maintain any variations of the probe light shift and Zeeman shift below the 1×10^{-17} (4.3 mHz) level, the clock laser beam power and the current $i_{B,0}$ in the bias field coils are actively stabilized.

For stabilization of the clock laser power, we use a combination of an analog and a digital power stabilization, acting on the RF power feeding an acousto-optic frequency shifter in the clock laser breadboard. The digital stabilization serves as integrator of the analog error signal, spanning several experimental cycles. It minimizes lock errors of the analog servo when the beam is turned on. With this system, we can achieve a long-term beam power fractional instability below 1×10^{-3} over a few days, corresponding to $<2 \times 10^{-18}$ for the fractional shift, for our interrogation parameters.

The current stabilization is based on a digital multimeter (DMM) measuring the current; the DMM reading is fed into a digital PID control, which steers the external control voltage of the power supply once every clock cycle. Based on the DMM's specifications, the expected fractional instability of the second-order Zeeman shift, using $T_\pi = 4$ s and $i_{B,0} = +215$ mA, is below 2×10^{-4} (over 24 h), corresponding to a 3.1×10^{-18} uncertainty on the frequency shift.

To determine the clock's instability, it was compared to the fermionic ^{87}Sr clock at PTB [22,53]. Although the clock lasers of both systems are prestabilized to the same cryogenic silicon cavity, they are steered to the respective atomic references and thus independent on long timescales ($\tau > 200$ s). The combined instability is $4.1 \times 10^{-16}/\sqrt{\tau/\text{s}}$ and averages down to the 3×10^{-18} level (Fig. 4). A number of measurements were acquired over the time span of a few months with similar results.
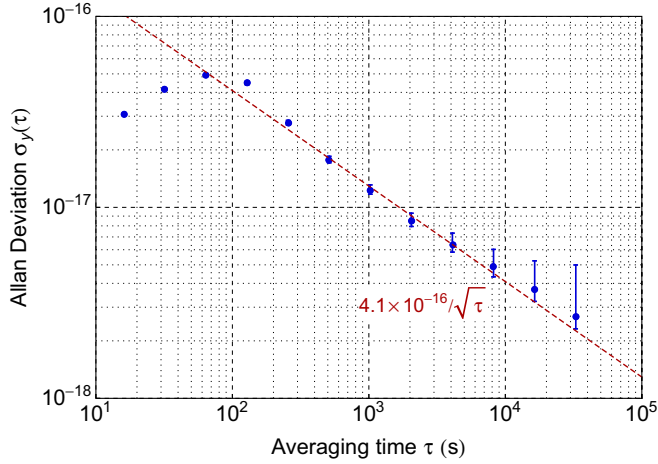
FIG. 4. Allan deviation of the fractional frequency offset between the ^{88}Sr clock and the PTB ^{87}Sr clock.

C. Evaluation of the systematic shifts

Table I summarizes the uncertainty budgets of the bosonic and fermionic clocks [22]. The systematic shifts of the clock were controlled and determined in the following way.

1. Blackbody radiation (BBR) shift

For the evaluation of the BBR shift, the temperature of the chamber is monitored by 17 temperature sensors (ten of them on the chamber windows). Thanks to the small size of the chamber and of the MOT coils, a passive cooling system based on heat pipes is sufficient for dissipating most of the heat ($\simeq 8$ W) produced by the MOT coils. We do not use an active temperature stabilization, but rely on the high stability of the laboratory temperature. The resulting difference between the warmest ($T_{\max}$) and coldest point ($T_{\min}$) of the vacuum chamber is between 250 and 400 mK, depending on operational parameters. Assuming a uniform probability distribution for the temperature experienced by the atoms, the representa-

TABLE I. Uncertainty budgets for the ^{88}Sr and ^{87}Sr clocks. Columns 2, 4: fractional shift (experimental minus unperturbed frequency) or the differential fractional gravitational shift (^{88}Sr clock)–(^{87}Sr clock); column 3, 5: fractional uncertainties of the shifts. All numbers are to be multiplied by 10^{-17}.

Effect	^{88}Sr clock		^{87}Sr clock	
	$\Delta\nu/\nu$	u/ν	$\Delta\nu/\nu$	u/ν
BBR shift	−523.4	0.8	−492.2	1.5
BBR oven shift	0	0	−0.9	0.9
Lattice shift ($\Delta\nu_L$)	−1.8	1.1	−0.9	0.4
Probe light shift ($\Delta\nu_P$)	−96.1	1.3	0.0	0.0
Cold collision shift ($\Delta\nu_{LP}$)	−0.6	0.3	0.0	0.2
Second-order Zeeman shift ($\Delta\nu_B$)	−209.7	0.5	−3.4	0.1
Tunneling	0	0	0.0	0.3
Background gas collision shift	−0.13	0.13	−0.8	0.8
dc-stark shift	−0.2	0.2	−0.2	0.1
Gravitational shift	+5.1	0.1	0.0	
Total shift	−826.9	2.0	−498.4	2.0

tive temperature is $T_{\text{avg}} = (T_{\max} + T_{\min})/2$ with uncertainty $(T_{\max} - T_{\min})/\sqrt{12}$ [54]. The BBR shift is computed using the coefficients from Refs. [55,56]. The calibration uncertainty of the temperature sensors (15 mK) is not significant for the uncertainty evaluation. An atomic beam shutter upstream from the atom chamber is closed during the atom interrogation cycle and shields the atoms from the BBR emitted by the oven.

An additional contribution arises from BBR transmitted by the windows. In particular, there are two large windows (BK-7, diameter 35 mm, thickness $t = 3$ mm) close to the atoms, which subtend a solid angle of $\Omega^{(w)} \simeq 0.4 \times 4\pi$. They face the inner sides of the MOT coils, which are usually warmer than the chamber during operation.

The BBR transmitted by the windows can be estimated using the spectral absorption coefficient $a(\nu)$ of BK-7 glass, which we have estimated from Ref. [57], and transmission measurements performed at PTB Berlin. The spectral power density of the BBR field inside the chamber is

$$S_{\text{BBR}}^{(\text{eff})}(\nu, T_e, T_{\text{avg}}) = S_{\text{BBR}}(\nu, T_{\text{avg}}) + \Delta S_{\text{BBR}}^{(w)}(\nu, T_e, T_{\text{avg}}),$$

with $S_{\text{BBR}}(\nu, T)$ the power spectral density according to Planck's law and

$$\Delta S_{\text{BBR}}^{(w)}(\nu, T_e, T_{\text{avg}}) = e^{-a(\nu)t}(S_{\text{BBR}}(\nu, T_e) - S_{\text{BBR}}(\nu, T_{\text{avg}})),$$

where we assume that the transmitted BBR extends over a solid angle of 4π. If we take into account the reduction of the subtended solid angle by the inner walls of the vacuum chamber and reflection of the transmittted BBR inside the vacuum chamber, similar to Ref. [58], we find that $\Delta S_{\text{BBR}}^{(w)}$ is not modified substantially in our case, as long as the absorption coefficient of the inner walls is small. Therefore, to obtain an upper limit, we assume the modification $\Delta S_{\text{BBR}}^{(w)}(\nu, T_e, T_{\text{avg}})$ applies in full.

The resulting modification of the BBR frequency shift is given by

$$\Delta\nu_{\text{BBR}}^{(w)} = \frac{1}{2hc\epsilon_0} \int_0^\infty \Delta\alpha(\nu)\Delta S_{\text{BBR}}(\nu, T_e, T_{\text{avg}})d\nu,$$

where $\Delta\alpha(\nu) = \alpha_e(\nu) - \alpha_g(\nu)$ is the difference of the frequency-dependent polarizabilities of the two clock states, with the low-frequency value $\Delta\alpha(0) = 4.07873(11) \times 10^{-39}$ m^2 C/V [55]. Figure 5 shows the modification $\Delta S_{\text{BBR}}^{(w)}$ of the BBR power spectrum for the exemplary conditions, and the differential polarizability $\Delta\alpha(\nu)$. We measured $T_e - T_{\text{avg}} = 0.5(3)$ K in our apparatus, and obtain $\Delta\nu_{\text{BBR}}^{(w)}/\nu_0 = -2.3(14) \times 10^{-19}$ as an upper limit, where the uncertainty results from the uncertainty of $T_e - T_{\text{avg}}$, and we used a linear approximation of the frequency shift around T_e. Here, we have numerically evaluated the integral up to a frequency of 150 THz; the contribution from BBR at higher frequencies has been confirmed to be negligible. Since we expect the reduction of $\Delta S_{\text{BBR}}^{(w)}$ by the inner walls to be small, we use this as the shift correction due to transmission through the windows. It is negligible compared to the BBR shift given in Table I. The effects of the slower laser beam entrance window (Fig. 2) and of the atomic beam shutter located in front of the oven are also negligible.
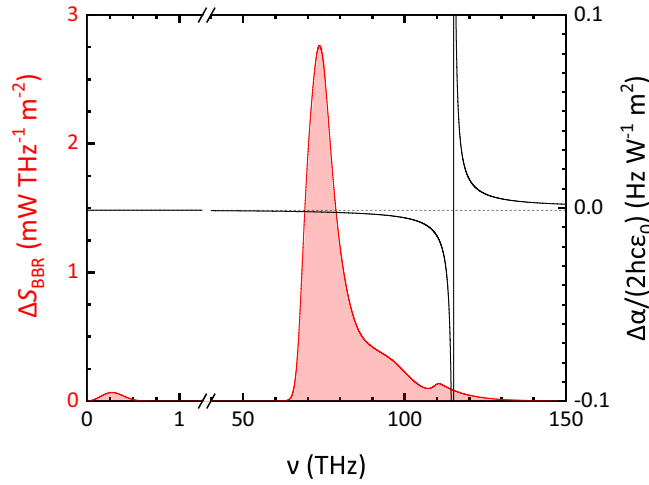
FIG. 5. Red line: modification $\Delta S_{\mathrm{BBR}}^{(\mathrm{w})}(\nu)$ of the spectral power density of black-body radiation, caused by transmission from an external environment at the temperature $T_{\mathrm{e}} = 300.5$ K through a 3-mm-thick BK-7 window at a temperature of $T_{\mathrm{avg}} = 300$ K. The effectively subtended solid angle of the radiation transmitted through the window is assumed to be 4π. Black: differential atomic polarizability $\Delta\alpha(\nu)/(2hc\epsilon_0)$, expressed as a normalized frequency shift, as a function of frequency ν. The additional frequency shift resulting from the BBR modification is $\Delta\nu_{\mathrm{BBR}}^{(\mathrm{w})}/\nu_0 = -2.3 \times 10^{-19}$ for this value of T_e.

2. Lattice light shift

We measured this shift at lattice depths of 100 E_{r} and 157 E_{r} ($E_{\mathrm{r}} = h^2/(2m\lambda_{\mathrm{lat}}^2)$ is the lattice photon recoil energy), while the operating value is 129 E_{r}. These comparatively high values are necessary to create a large trap volume (i.e., obtain a large number of sites in longitudinal direction). This in turn allowed us to reduce the atom density and thus the collisional effects (see below and Appendix B). For the lattice light shift evaluation, we used the expression given by [46]

$$
\Delta\nu_{\mathrm{L}} = \zeta\left(n + \frac{1}{2}\right)\left(\frac{U_0}{E_{\mathrm{r}}}\right)^{1/2}
$$
$$
- \left(\frac{\partial\Delta\alpha^{\mathrm{E1}}}{\partial\nu}\Delta\nu_{\mathrm{lat,m}} + \frac{3}{4}\Delta k_{\mathrm{H}}(2n^2 + 2n + 1)\right)\frac{U_0}{E_{\mathrm{r}}}
$$
$$
+ \Delta k_{\mathrm{H}}(2n + 1)\left(\frac{U_0}{E_{\mathrm{r}}}\right)^{3/2} - \Delta k_{\mathrm{H}}\left(\frac{U_0}{E_{\mathrm{r}}}\right)^2, \qquad (1)
$$

where $\zeta = (\partial\Delta\alpha^{\mathrm{E1}}/\partial\nu)\Delta\nu_{\mathrm{lat,m}} - \Delta\alpha^{\mathrm{E2,M1}}$, with $\Delta\alpha^{\mathrm{E1}}$ the normalized differential electric-dipole polarizability, ν_{lat} the lattice frequency, $\Delta\nu_{\mathrm{lat,m}}$ the detuning of the lattice frequency from the magic value, and $\Delta\alpha^{\mathrm{E2,M1}} = (\alpha_{\mathrm{e}}^{\mathrm{E2}} + \alpha_{\mathrm{e}}^{\mathrm{M1}}) - (\alpha_{\mathrm{g}}^{\mathrm{E2}} + \alpha_{\mathrm{g}}^{\mathrm{M1}}) = 0.0(3)$ mHz [45] the normalized differential multipolar polarizability. The partial derivative of the differential dipole polarizability is $\partial\Delta\alpha^{\mathrm{E1}}/\partial\nu = 19.3 \times 10^{-12}$ (Hz Hz^{-1}) [46], n is the axial quantum number, and U_0 is the effective trap depth, which takes into account the excitation of atomic motion in radial direction. Δk_{H} is the (normalized) hyperpolarizability coefficient for linear lattice polarization, whose most accurate published value is $-0.45(10)$ μHz [59].

The lattice light shift is measured by operating the clock at two different lattice depths (shallow and deep lattice)

on subsequent trap loading cycles (interleaved operation). The difference in the transition frequency is measured with a fractional uncertainty of 6.5×10^{-18}, after $\sim$10 000 s of averaging. From this measurement, we obtain the detuning from the magic wavelength $\Delta\nu_{\mathrm{lat,m}} = 8(10)$ MHz by solving Eq. (1). Sideband spectroscopy was used to determine the axial temperature (average quantum number $\langle n\rangle \approx 1.4$) and the lattice depth $U_0 = 129$ E_{r}. All other parameters are known. The lattice shift is then evaluated for U_0 using Eq. (1) and is reported in Table I.

The magic frequency is $\nu_{\mathrm{lat,m}} = 368\,554\,753(11)$ MHz, 1.8 σ lower than the value reported in Ref. [26] (368 554 778(8) MHz), with σ the combined uncertainty of the two measurements.

3. Second-order Zeeman shift

We first cancel the residual magnetic field components in the x and y directions, perpendicular to the bias field $B\hat{z}$. This is done by applying additional magnetic fields in these directions using two pairs of compensation coils and evaluating the resulting frequency shifts as a function of the applied fields: The perpendicular fields are compensated by setting the current in the coils to the values that minimize the shifts (minimum of the parabolic fits). The uncertainty of the compensation procedure adds an uncertainty of 1.3×10^{-18} to the second-order Zeeman shift correction. See Appendix A for details.

Afterwards, the same measurement is repeated for evaluating the second-order Zeeman shift induced by the coupling field B (parallel to the lattice polarization axis). Figure 6 shows the measurement of the second-order Zeeman shift induced by the coupling field $B\hat{z}$. Each point is acquired from an interleaved measurement, with two different currents, $i_{\mathrm{B,0}}$ (reference current) and $i_{\mathrm{B,}z}$. A system of switches allows inverting the current in the coils. The interrogation
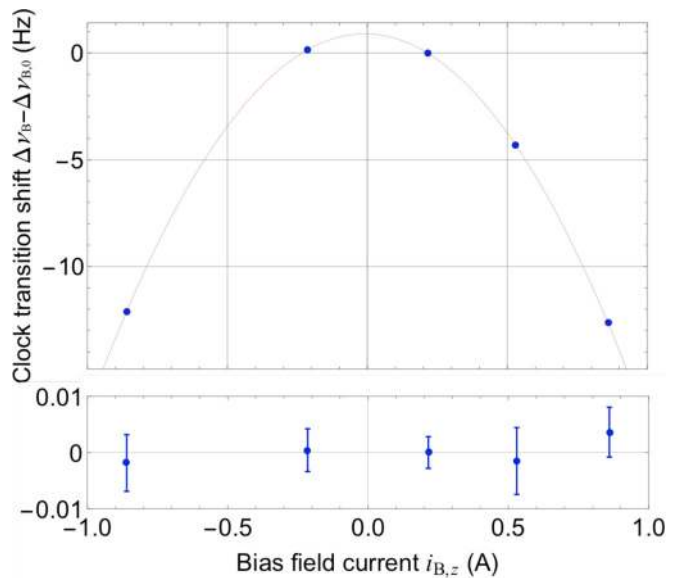

FIG. 6. Second-order Zeeman shift with respect to the shift at the operating point $i_{\mathrm{B,0}} = +215$ mA, and fit residuals. The shift at the operating conditions is $\Delta\nu_{\mathrm{B,0}} = -900.2(22)$ mHz.
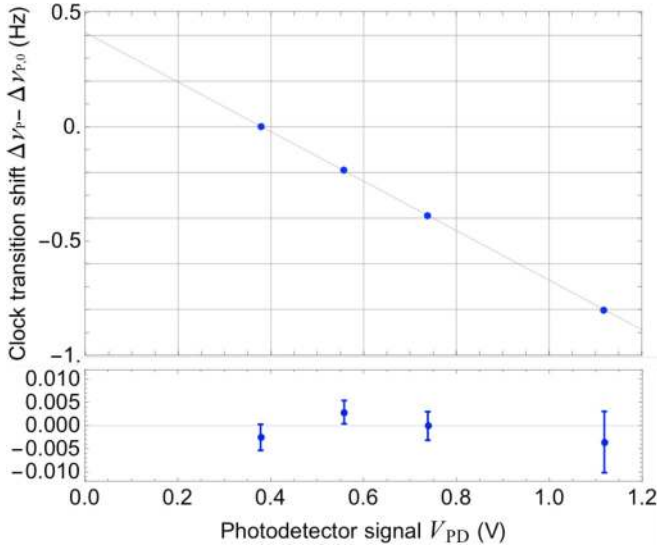
FIG. 7. Measurement of the probe light shift relative to the value at the operating power, corresponding to a PD signal $V_{PD,0} = 378$ mV, and fit residuals.

time T_π is set to match the different Rabi frequencies of the cycles. The data are fit with the function $\Delta \nu_B - \Delta \nu_{B,0} = \gamma((i_{B,0} - i_{0,z})^2 - (i_{B,z} - i_{0,z})^2)$, where $\Delta \nu_{B,0}$ is the shift at the reference current and $i_{0,z}$ is the unknown current necessary to compensate for the external offset field in z direction (maximum of the parabola). We find $i_{0,z} = -0.009(2)$ A and $\gamma = 17.94(1)$ Hz/A^2. Thus, the shift at the reference current $i_{B,0}$ is $\Delta \nu_{B,0} = \gamma(i_{0,z} - i_{B,0})^2 = -900.2(22)$ mHz ($\simeq -2.1 \times 10^{-15}$) (see Table I).

In case the axes of the compensation coils are not perfectly perpendicular to $\hat{z}$, a small residual offset field may exist in the x and y directions. It is not compensated in this procedure. The corresponding additional shift is evaluated to be $\ll 1 \times 10^{-18}$ (Appendix A).

Finally, the effect caused by instability of the current in the coils and of the background field is negligible at the 1×10^{-18} level (Appendix A).

4. Probe light shift

The probe light shift is measured similarly to the second-order Zeeman shift (Fig. 7) by applying different clock laser intensities and measuring the corresponding changes in the clock transition frequency. Since the Rabi frequency is changed when the intensity is varied, we fulfill the π-pulse condition by adapting T_π. The data are fit with a linear function. At the operating value of the intensity around $I_0 \approx 28$ mW/cm^2, the measurement yields a shift $\Delta \nu_{P,0} = -413.0(53)$ mHz ($\simeq -9.6 \times 10^{-16}$). The difference compared with the expected shift of -0.50 Hz is attributed to the uncertainty of the intensity stabilization photodetector's calibration, and to nonperfect overlap between the clock and the lattice beam.

5. Density (cold collision) shift

To evaluate the cold collision shift, we introduce an approach based on a line-shape analysis. Figure 8(a) shows a
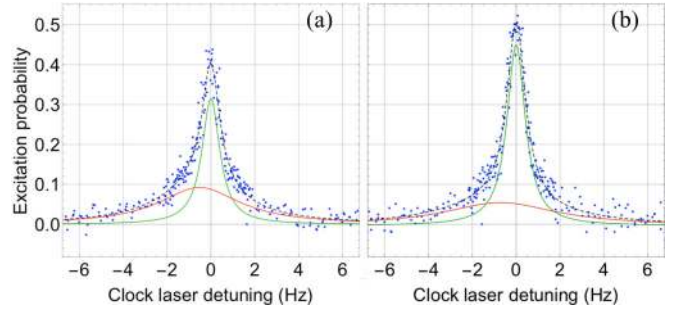

FIG. 8. Clock transition scans acquired with $T_\pi = 1.0$ s interrogation time (a) with detuned PA laser applied before each atom interrogation and (b) with resonant PA laser. The black dashed curve is the fit function including a line from singly occupied sites (green) and a line from multiply occupied sites (red).

clock transition scan obtained with $T_\pi = 1.0$ s interrogation time. We model the line shape as a sum of two Lorentzian profiles: the main one (green) resulting from atoms in singly occupied lattice sites, its width being close to the Fourier limit. The second profile (red) results from atoms in multiply occupied lattice sites. It has a broader width and a negative frequency shift [40]. This phenomenological model is an approximation; for a fermionic clock, a theoretical description matching the experimental data was presented in Ref. [60].

We verify the model using the technique of photoassociation (PA) [61] to remove atoms from multiply occupied lattice sites. Figure 8(b) is a scan obtained with the same interrogation parameters but applying PA before interrogation to confirm the origin of the broader profile. During the PA process, pairs of atoms in the same lattice site form excited Sr$_2$ molecules by absorbing a photon from the PA beam. The molecules decay with high probability into two hot atoms each, which are lost from the lattice. In this way, the fraction of multiply occupied sites is reduced. The PA transition is driven by radiation detuned by about -222 MHz from the $^1S_0 \rightarrow {}^3P_1$ transition [26] (689 nm, obtained from the same laser as employed in the laser cooling), with an intensity of about 1 W/cm^2, for 600 ms before the clock interrogation. In the scan Fig. 8(a), the PA beam is not actually off, but its frequency is detuned by a few MHz from the PA transition. This ensures that all disturbances due to the PA beam (such as atom heating), except for the PA process itself, are equal to the situation in scan Fig. 8(b), where the PA laser is tuned on-resonance. Comparison of Figs. 8(a) and 8(b) confirms the model: the contribution of the profile from multiply occupied sites (red) is reduced when PA is applied, and the peak strength increases. The fact that this contribution is not fully canceled may be explained by excited molecules decaying into the internal ground state and remaining trapped in sites that were originally occupied by three or more Sr atoms. These could then lead to collisional broadening and shifts.

We can assume that the main profile (green) represents the unperturbed transition (i.e., atoms not affected by collisions) and evaluate the collisional shift as the line pulling due to the second profile. Furthermore, to be less sensitive to this line pulling, the main profile interrogation is done experimentally at two detunings closer to the center of the

main profile than at half height. The resulting line pulling during the measurement of the $^{88}\mathrm{Sr}-^{87}\mathrm{Sr}$ isotope shift is $\Delta \nu_{\mathrm{LP}} = 2.5(15)$ mHz ($5.7(34) \times 10^{-18}$). The uncertainty of this shift is rather small if compared with the total clock uncertainty. Therefore, this does not represent a critical point for the isotope shift evaluation performed in the present work. In the future, once all the uncertainties on the other systematic shifts will be reduced to similarly low values, the evaluation of the collisional shift using this model needs to be readdressed with a more in-depth analysis.

We have also performed the standard collision shift characterization by varying the number of atoms in the lattice and arrive at a similar result (Appendix B).

6. dc Stark shift

This effect is a potential issue, since the small size of the vacuum chamber places the nonconductive chamber windows, a potential location of accumulated electric charges, as close as 7 mm to the atoms. The shift is measured by applying voltages, in turn, to three pairs of approximately circular wire electrodes placed externally to the windows, and measuring the resulting clock transition frequency shift. From the quadratic fit, the residual shift for the operating condition of zero applied voltages is $2(2) \times 10^{-18}$.

7. Background gas collision shift

It can be evaluated, as reported in Ref. [62], from the lattice lifetime and using the coefficients given in Ref. [63], that the measured lattice lifetime is 5.6 s, leading to a shift of $-1.3(13) \times 10^{-18}$.

8. Tunneling shift

Given the average occupation number, $\langle n \rangle \approx 1.4$, as evaluated from sideband spectroscopy, the relatively deep lattice of $129\ E_{\mathrm{r}}$, and considering the vertical orientation of the lattice
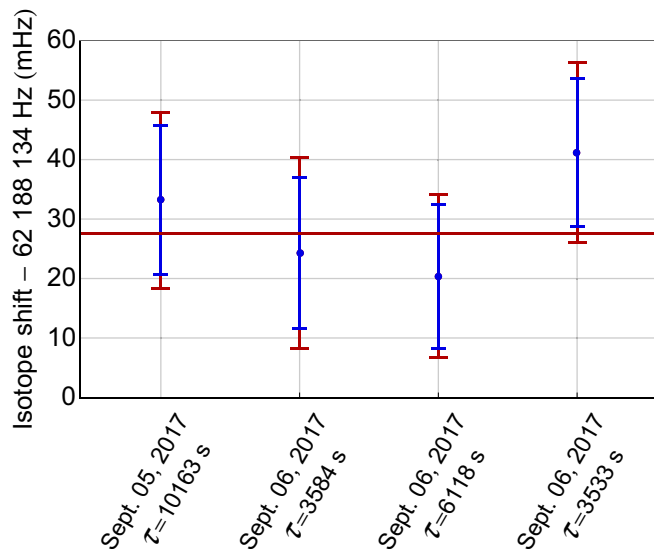

FIG. 9. Measurement used for the evaluation of the isotope shift value (red line). The blue and red error bars represent the systematic and total uncertainty, respectively.
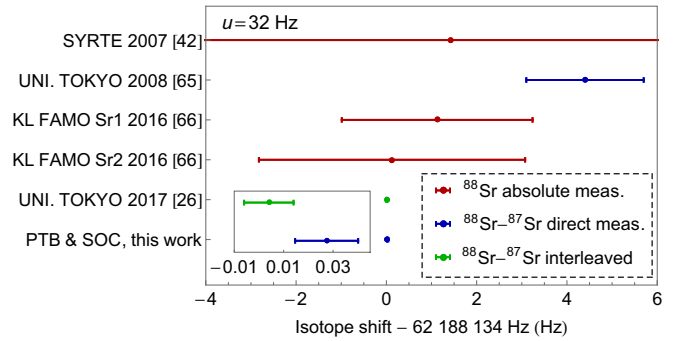

FIG. 10. Present isotope shift, compared with published values [65,66]. The left inset box shows the two most recent measurements results on a ∼50-fold enlarged scale.

beams, we calculate, according to Ref. [64], that the shift due to tunneling is negligible.

V. MEASUREMENT OF THE BOSON-FERMION ISOTOPE SHIFT

For the evaluation of the isotope shift, we used the average of four measurements comparing the OLC with the PTB clock (Fig. 9), acquired over two days.

The lattice shift, probe light shift, and the Zeeman shift measurements were acquired on the same days. The resulting $^{88}\mathrm{Sr}-^{87}\mathrm{Sr}$ isotope shift is 62 188 134.027(12) Hz, where the uncertainty (12 mHz) corresponds to 3.0×10^{-17}. The uncertainty arises from the bosonic clock's uncertainty, the PTB clock's uncertainty, and the statistical uncertainty of the frequency comparison (1.1 mHz). In Fig. 10, our measurement is compared with previously published values. In particular, it agrees with the value recently reported in Ref. [26] within 2σ of the combined uncertainty of both measurements.

During the measurement of the isotope shift, no PA beam was used. However, the atoms were loaded into the lattice starting from a red MOT with higher temperature and larger size, meaning lower density, spreading the atoms over more lattice sites. Since we ran the system with an atom number between a few hundred and a thousand, and the number of lattice sites was of the order of 10^3, we estimate that we had less than one atom per lattice site, on average. In addition, the long interrogation time provided narrower transition lines than depicted in Fig. 8 from singly occupied sites and thus reduced the effect of line pulling.

VI. CONCLUSION AND OUTLOOK

In conclusion, we have demonstrated a bosonic OLC with 3×10^{-18} instability and 2.0×10^{-17} uncertainty. This result was obtained by operating the clock with long interrogation times of 4 s, with suitably low atom density, stabilizing the important physical parameters of the apparatus by active control, and accurate evaluation of the shifts. The long interrogation time was only possible by exploiting the ultralow instability of a cryogenic reference cavity [43]. We thus realize the long-predicted potential of bosonic OLCs, with a factor of approximately 30 improvement in terms of accuracy and instability compared with the best values reported so far [26].

An actual measurement of a physical quantity, the ^{88}Sr$-^{87}$Sr isotope shift, was performed with the OLC. Our result is in agreement with another recent result [26]. To the best of our knowledge, the obtained frequency ratio [67]

$$f(^{88}\text{Sr})/f(^{87}\text{Sr}) = 1.000\,000\,144\,883\,682\,831(28)$$

is among the most precisely determined properties of nature, and is also one of the most precise measurements in physics, understood as the comparison of a system's property with the analogous one of a reference system (compare with, e.g., Ref. [18,26]).

We see significant potential for improving the bosonic OLC approach further by achieving a longer atom lifetime in the lattice and implementing, for instance, higher-dimensional lattices, hyper-Ramsey or auto-balanced-Ramsey spectroscopy [68,69]. Bosonic clocks may then become competitive with fermionic ones, and relevant for applications where simplicity, reliability, or particular fundamental physics issues are essential. The presented technique should also be applicable to other species (Yb, Mg), which have values of $|\Delta\nu_\text{P} + \Delta\nu_\text{B}|_\text{min}$ similar to Sr [35].

The reported results were obtained with a Ti:sapphire lattice laser. We have also measured the ^{88}Sr$-^{87}$Sr isotope shift using a diode laser with tapered amplifier, combined with a grating filter [70]. This type of laser system is much better suited for space use because of its significantly smaller mass, volume, and power consumption. The result, 62 188 134.006(15) Hz, is within $1.3\,\sigma$ of the combined error of the two measurements with different lasers.

The present work shows that an OLC of compact size and tenfold improved inaccuracy compared to a microwave cold-atom clock is feasible. The work also indicates that an OLC with physical parameters suitable for accommodation on the ISS as an external payload and having low-10^{-17}-level uncertainty is feasible. Based on our experience with the presented SOC OLC, we have developed a preliminary design for a space OLC. It features a volume of 0.5 m^3, a power consumption of 250 W, and a mass of 100 kg (including electronics), and is capable of operating within the stated specifications over the large baseplate temperature range in orbit (0–45 °C) [31].

The production of a hardware model of this design will be the next development step. A complementary activity, currently ongoing within an ESA program, is the development of a high-performance space-compatible reference cavity for the clock laser. According to the I-SOC science case, its performance should be such that the clock laser frequency instability at the location of the trapped atoms will be at the 2×10^{-16} level, after subtraction of linear drift.

APPENDIX A: SECOND-ORDER ZEEMAN SHIFT MEASUREMENT

Before measuring the shift induced by the field component along the z axis, we compensate for the offset fields components along the x and y axes. As mentioned in the main text, this is done by repeating the second-order Zeeman shift measurement, using two pairs of compensation coils with axes perpendicular to $\hat{z}$, and finally setting their currents to the values that minimizes the shift. It is important that the compensation of the perpendicular magnetic fields is done before the measurement of the shift induced by the coupling field B: in case the field produced by the compensation coils at the atom position is not perfectly perpendicular to B (i.e., to $\hat{z}$), a change of the current in the x and y compensation coils would result in a change of the offset field in the z direction (and, consequently, of the parameter $i_{0,z}$ in the fit function).

If the field produced by the x- and y-compensation coils is not perfectly perpendicular to the direction of the coupling field $B\hat{z}$, an additional issue is introduced that is depicted in Fig. 11.

B_BG is the background offset field and x' is the direction of the field $B_{x'}$ produced by the x-compensation coils. x' is misaligned by an angle α from the x direction. By minimizing the second-order Zeeman shift as a function of the field produced by x-compensation coils, only the component $B_{\text{BG},x'}$ of the background field is nulled. The remaining component
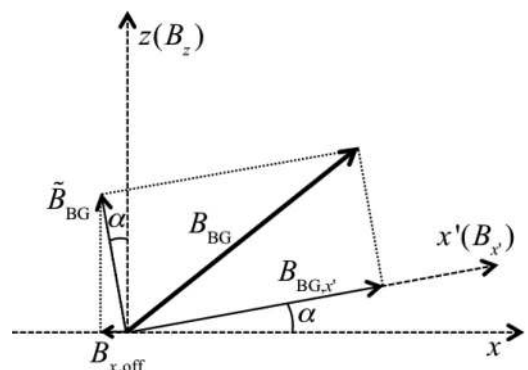

FIG. 11. Schematic of the magnetic field components for the second-order Zeeman shift measurement. Details are given in the text.

$\tilde{B}_{BG}$ introduces a residual offset field $B_{x,off}$ along the x axis, which results in a residual shift. To estimate $B_{x,off}$, we evaluate the angle α. For this purpose, we determine $B_{z,off}$ (offset field in z direction) as function of $B_{x'}$. This is done by measuring the quadratic Zeeman shift for two opposite values of B (bias field in z direction) and for $B_{x'} = 0$ and $B_{x'} = B_{x',max}$. We obtain $B_{x,off} = B_{z,off} / \tan \alpha$ and, from that, the residual shift. The same is repeated for the y direction. In both cases, the residual shift is much smaller than 1×10^{-18}. If these remaining shifts were larger, they could be further reduced by iteration of the compensation procedure.

The instability of the Zeeman shift could be a potential contribution to the measurement uncertainty. There are two aspects here: the stability of the current and the stability of the background field. From the fit, we obtain a sensitivity of 8 mHz/mA at the operating point ($i_{B,0} = 0.215$ A). 1 mA corresponds to about 1 μT. The current stabilization system provides an instability below 40 μA over a few days, corresponding to 0.4 mHz (9×10^{-19}). As an estimate for the instability of the background magnetic field, we monitor the linear Zeeman effect of the ^{87}Sr lattice clock, which is located less than 10 m from the ^{88}Sr apparatus. Using the Zeeman coefficient from Ref. [71], we observe that background field variations are smaller than 5×10^{-8} T, which is small enough to ensure that the uncertainty of the correction is negligible at low 10^{-18} level for the second-order Zeeman effect. These and other possible disturbing effects (e.g., eddy currents) may introduce a linear component in the fit of Fig. 11, but none was found to be necessary.

APPENDIX B: COLD COLLISIONAL SHIFT: "STANDARD" DETERMINATION

In addition to the evaluation of the collisional shift from line pulling (see main text), we also performed a "standard" measurement, varying the number of atoms trapped in the lattice by changing the Zeeman slower beam power. We make
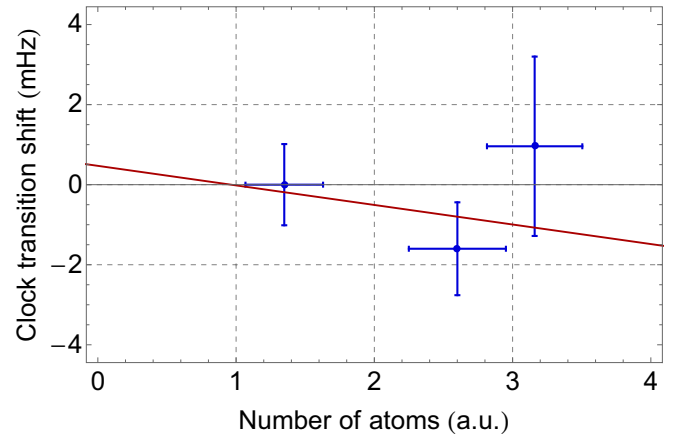

FIG. 12. Determination of the collisional shift. For the uncertainty on the atom number the standard deviation of the PMT signals is used.

sure that the trap parameters do not change significantly by acquiring and comparing the sideband spectrum corresponding to the different number of atoms. Due to the line broadening occurring at higher atomic densities, it is not possible to significantly increase the atom number compared to the operating value. This limits the range of data available for the shift determination. The measurement is performed by running the clock with a single atomic servo (i.e., not in interleaved mode) and using the PTB Sr clock as flywheel. Figure 12 shows the result. During the measurement at the lowest atom number (leftmost data point) the number of atoms is actively stabilized, by correcting appropriately the 461 nm slower wave power. From a fit to the data, the cold collisional shift for the atom number under operating conditions is 0.5(22) mHz ($1(5) \times 10^{-18}$), consistent with the result obtained with the line-pulling evaluation described in the main text, 2.5(15) mHz, or $6(3) \times 10^{-18}$.

[1] H. Katori, M. Takamoto, V. G. Pal'chikov, and V. D. Ovsiannikov, Phys. Rev. Lett. **91**, 173005 (2003).

[2] A. Derevianko and H. Katori, Rev. Mod. Phys. **83**, 331 (2011).

[3] N. Poli, C. W. Oates, P. Gill, and G. M. Tino, Riv. del Nuovo Cimento **36**, 555 (2013).

[4] A. D. Ludlow, M. M. Boyd, J. Ye, E. Peik, and P. O. Schmidt, Rev. Mod. Phys. **87**, 637 (2015).

[5] M. Schioppo, R. C. Brown, W. F. McGrew, N. Hinkley, R. J. Fasano, K. Beloy, T. H. Yoon, G. Milani, D. Nicolodi, J. A. Sherman, N. B. Phillips, C. W. Oates, and A. D. Ludlow, Nat. Photonics **11**, 48 (2017).

[6] W. F. McGrew, X. Zhang, R. J. Fasano, S. A. Schäffer, K. Beloy, D. Nicolodi, R. C. Brown, N. Hinkley, G. Milani, M. Schioppo, T. H. Yoon, and A. D. Ludlow, arXiv:1807.11282.

[7] D. Calonico, E. K. Bertacco, C. E. Calosso, C. Clivati, G. A. Costanzo, M. Frittelli, A. Godone, A. Mura, N. Poli, D. V. Sutyrin, G. Tino, M. E. Zucco, and F. Levi, Appl. Phys. B **117**, 979 (2014).

[8] T. Takano, M. Takamoto, I. Ushijima, N. Ohmae, T. Akatsuka, A. Yamaguchi, Y. Kuroishi, H. Munekane, B. Miyahara, and H. Katori, Nat. Photonics **10**, 662 (2016).

[9] C. Lisdat, G. Grosche, N. Quintin, C. Shi, S. Raupach, C. Grebing, D. Nicolodi, F. Stefani, A. Al-Masoudi, S. Dörscher, S. Häfner, J.-L. Robyr, N. Chiodo, S. Bilicki, E. Bookjans, A. Koczwara, S. Koke, A. Kuhl, F. Wiotte, F. Meynadier, E. Camisard, M. Abgrall, M. Lours, T. Legero, H. Schnatz, U. Sterr, H. Denker, C. Chardonnet, Y. Le Coq, G. Santarelli, A. Amy-Klein, R. Le Targat, J. Lodewyck, O. Lopez, and P.-E. Pottie, Nat. Commun. **7**, 12443 (2016).

[10] K. Predehl, G. Grosche, S. M. F. Raupach, S. Droste, O. Terra, J. Alnis, T. Legero, T. W. Hänsch, T. Udem, R. Holzwarth, and H. Schnatz, Science **336**, 441 (2012).

[11] F.-L. Takamotoawa, K. Watabe, T. Ikegami, M. Imae, Y. Fujii, M. Amemiya, K. Nakagawa, K. Ueda, and H. Katori, Opt. Lett. **34**, 692 (2009).

[12] A. Yamaguchi, M. Fujieda, M. Kumagai, H. Hachisu, S. Nagano, Y. Li, T. Ido, T. Takano, M. Takamoto, and H. Katori, Appl. Phys. Express **4**, 082203 (2011).

[13] H. Hachisu, M. Fujieda, S. Nagano, T. Gotoh, A. Nogami, T. Ido, S. Falke, N. Huntemann, C. Grebing, B. Lipphardt, C. Lisdat, and D. Piester, Opt. Lett. **39**, 4072 (2014).

[14] M. Takamoto, I. Ushijima, M. Das, N. Nemitz, T. Ohkubo, K. Yamanaka, N. Ohmae, T. Takano, T. Akatsuka, A. Yamaguchi, and H. Katori, C. R. Phys. **16**, 489 (2015).

[15] J. Grotti, S. Koller, S. Vogt, S. Häfner, U. Sterr, C. Lisdat, H. Denker, C. Voigt, L. Timmen, A. Rolland, F. N. Baynes, H. S. Margolis, M. Zampaolo, P. Thoumany, M. Pizzocaro, B. Rauf, F. Bregolin, A. Tampellini, P. Barbieri, M. Zucco, G. A. Costanzo, C. Clivati, F. Levi, and D. Calonico, Nat. Phys. **14**, 437 (2018).

[16] M. E. Tobar, P. L. Stanwix, J. J. McFerran, J. Guéna, M. Abgrall, S. Bize, A. Clairon, P. Laurent, P. Rosenbusch, D. Rovera, and G. Santarelli, Phys. Rev. D **87**, 122004 (2013).

[17] P. Delva, J. Lodewyck, S. Bilicki, E. Bookjans, G. Vallet, R. Le Targat, P.-E. Pottie, C. Guerlin, F. Meynadier, C. Le Poncin-Lafitte, O. Lopez, A. Amy-Klein, W.-K. Lee, N. Quintin, C. Lisdat, A. Al-Masoudi, S. Dörscher, C. Grebing, G. Grosche, A. Kuhl, S. Raupach, U. Sterr, I. R. Hill, R. Hobson, W. Bowden, J. Kronjäger, G. Marra, A. Rolland, F. N. Baynes, H. S. Margolis, and P. Gill, Phys. Rev. Lett. **118**, 221102 (2017).

[18] T. Rosenband, D. B. Hume, P. O. Schmidt, C. W. Chou, A. Brusch, L. Lorini, W. H. Oskay, R. E. Drullinger, T. M. Fortier, J. E. Stalnaker, S. A. Diddams, W. C. Swann, N. R. Newbury, W. M. Itano, D. J. Wineland, and J. C. Bergquist, Science **319**, 1808 (2008).

[19] R. M. Godun, P. B. R. Nisbet-Jones, J. M. Jones, S. A. King, L. A. M. Johnson, H. S. Margolis, K. Szymaniec, S. N. Lea, K. Bongs, and P. Gill, Phys. Rev. Lett. **113**, 210801 (2014).

[20] N. Huntemann, B. Lipphardt, C. Tamm, V. Gerginov, S. Weyers, and E. Peik, Phys. Rev. Lett. **113**, 210802 (2014).

[21] J. Lodewyck, S. Bilicki, E. Bookjans, J. L. Robyr, C. Shi, G. Vallet, R. Le Targat, D. Nicolodi, Y. Le Coq, and J. Guéna, Metrologia **53**, 1123 (2016).

[22] C. Grebing, A. Al-Masoudi, S. Dörscher, S. Häfner, V. Gerginov, S. Weyers, B. Lipphardt, F. Riehle, U. Sterr, and C. Lisdat, Optica **3**, 563 (2016).

[23] H. Hachisu, F. Nakagawa, Y. Hanado, and T. Ido, Sci. Rep. **8**, 4243 (2018).

[24] S. B. Koller, J. Grotti, S. Vogt, A. Al-Masoudi, S. Dörscher, S. Häfner, U. Sterr, and C. Lisdat, Phys. Rev. Lett. **118**, 073601 (2017).

[25] C. Delaunay, R. Ozeri, G. Perez, and Y. Soreq, Phys. Rev. D **96**, 093001 (2017).

[26] T. Takano, R. Mizushima, and H. Katori, Appl. Phys. Express **10**, 072801 (2017).

[27] A. Derevianko and M. Pospelov, Nat. Phys. **10**, 933 (2014).

[28] L. Liu, D. Lü, W. Chen, T. Li, Q. Qu, B. Wang, L. Li, W. Ren, Z. Dong, J. Zhao, W. Xia, X. Zhao, J. Ji, M. Ye, Y. Sun, Y. Yao, D. Song, Z. Liang, S. Hu, D. Yu, X. Hou, W. Shi, H. Zang, J. Xiang, X. Peng, and Y. Wang, arXiv:1709.03256.

[29] M. P. Hess, L. Stringhetti, B. Hummelsberger, K. Hausner, R. Stalford, R. Nasca, L. Cacciapuoti, R. Much, S. Feltham, T. Vudali, B. Leger, F. Picard, D. Massonnet, P. Rochat, D. Goujon, W. Schäfer, P. Laurent, P. Lemonde, A. Clairon, P. Wolf,

[30] T. Lévèque, B. Faure, F. X. Esnault, C. Delaroche, D. Massonnet, O. Grosjean, F. Buffe, P. Torresi, T. Bomer, A. Pichon, P. Béraud, J. P. Lelay, S. Thomin, and P. Laurent, Rev. Sci. Instrum. **86**, 033104 (2015).

[31] S. Schiller, S. Origlia, M. S. Pramod, C. Lisdat, U. Sterr, M. Gellesch, Y. Singh, K. Bongs, I. Prochazka, N. Poli, G. M. Tino, R. Le Targat, J. Lodewyck, F. Levi, L. Cacciapuoti, and C. Moratto, ESA Phase-A Scientific Study I-SOC, ESTEC Contract No. 20579/ 07/ NL/VJ.

[32] S. Schiller and L. Cacciapuoti, I-SOC ESR document (2018).

[33] K. Bongs, Y. Singh, L. Smith, W. He, O. Kock, D. Świerad, J. Hughes, S. Schiller, S. Alighanbari, S. Origlia, S. Vogt, U. Sterr, C. Lisdat, R. Le Targat, J. Lodewyck, D. Holleville, B. Venon, S. Bize, G. P. Barwood, P. Gill, I. R. Hill, Y. B. Ovchinnikov, N. Poli, G. M. Tino, J. Stuhler, and W. Kaenders, C. R. Phys. **16**, 553 (2015).

[34] S. Origlia, S. Schiller, M. Pramod, L. Smith, Y. Singh, W. He, S. Viswam, D. Świerad, J. Hughes, K. Bongs, U. Sterr, C. Lisdat, S. Vogt, S. Bize, J. Lodewyck, R. Le Targat, D. Holleville, B. Venon, P. Gill, G. Barwood, I. R. Hill, Y. Ovchinnikov, A. Kulosa, W. Ertmer, E. M. Rasel, J. Stuhler, and W. Kaenders, Proc. SPIE **9900**, 990003 (2016).

[35] A. V. Taichenachev, V. I. Yudin, C. W. Oates, C. W. Hoyt, Z. W. Barber, and L. Hollberg, Phys. Rev. Lett. **96**, 083001 (2006).

[36] A. Y. Nevsky, S. Alighanbari, Q. Chen, I. Ernsting, S. Vasilyev, S. Schiller, G. Barwood, P. Gill, N. Poli, and G. M. Tino, Opt. Lett. **38**, 4903 (2013).

[37] D. Świerad, S. Häfner, S. Vogt, B. Venon, D. Holleville, S. Bize, A. Kulosa, S. Bode, Y. Singh, K. Bongs, E. M. Rasel, J. Lodewyck, R. Le Targat, C. Lisdat, and U. Sterr, Sci. Rep. **6**, 33973 (2016).

[38] M. Schioppo, N. Poli, M. Prevedelli, S. Falke, C. Lisdat, U. Sterr, and G. M. Tino, Rev. Sci. Instrum. **83**, 103101 (2012).

[39] I. R. Hill, Y. B. Ovchinnikov, E. M. Bridge, E. A. Curtis, and P. Gill, J. Phys. B **47**, 75006 (2014).

[40] C. Lisdat, J. S. R. Vellore Winfred, T. Middelmann, F. Riehle, and U. Sterr, Phys. Rev. Lett. **103**, 090801 (2009).

[41] T. Hong, C. Cramer, W. Nagourney, and E. N. Fortson, Phys. Rev. Lett. **94**, 050801 (2005).

[42] X. Baillard, M. Fouché, R. Le Targat, P. G. Westergaard, A. Lecallier, Y. Le Coq, G. D. Rovera, S. Bize, and P. Lemonde, Opt. Lett. **32**, 1812 (2007).

[43] D. G. Matei, T. Legero, S. Häfner, C. Grebing, R. Weyrich, W. Zhang, L. Sonderhouse, J. M. Robinson, J. Ye, F. Riehle, and U. Sterr, Phys. Rev. Lett. **118**, 263202 (2017).

[44] T. Mukaiyama, H. Katori, T. Ido, Y. Li, and M. Kuwata-Gonokami, Phys. Rev. Lett. **90**, 113002 (2003).

[45] P. G. Westergaard, J. Lodewyck, L. Lorini, A. Lecallier, E. A. Burt, M. Zawada, J. Millo, and P. Lemonde, Phys. Rev. Lett. **106**, 210801 (2011).

[46] H. Katori, V. D. Ovsiannikov, S. I. Marmo, and V. G. Palchikov, Phys. Rev. A **91**, 052503 (2015).

[47] C. Shi, J.-L. Robyr, U. Eismann, M. Zawada, L. Lorini, R. Le Targat, and J. Lodewyck, Phys. Rev. A **92**, 012516 (2015).

[48] S. Vogt, C. Lisdat, T. Legero, U. Sterr, I. Ernsting, A. Nevsky, and S. Schiller, Appl. Phys. B **104**, 741 (2011).

[49] S. Häfner, S. Falke, C. Grebing, S. Vogt, T. Legero, M. Merimaa, C. Lisdat, and U. Sterr, Opt. Lett. **40**, 2112 (2015).

[50] C. Hagemann, C. Grebing, T. Kessler, S. Falke, N. Lemke, C. Lisdat, H. Schnatz, F. Riehle, and U. Sterr, IEEE Trans. Instrum. Meas. **62**, 1556 (2013).

[51] S. Falke, M. Misera, U. Sterr, and C. Lisdat, Appl. Phys. B **107**, 301 (2012).

[52] G. J. Dick, in *Proceedings of 19th Annual Precise Time and Time Interval Meeting, Redondo Beach, 1987* (U.S. Naval Observatory, Washington, DC, 1988), pp. 133–147.

[53] A. Al-Masoudi, S. Dörscher, S. Häfner, U. Sterr, and C. Lisdat, Phys. Rev. A **92**, 063814 (2015).

[54] GUM, Guide to the Expression of Uncertainty in Measurement, (1995) (corrected and reprinted, 2008) in the name of the BIPM, IEC, IFCC, ISO, UPAC, IUPAP, and OILM (Sèrres, France, 1995).

[55] T. Middelmann, S. Falke, C. Lisdat, and U. Sterr, Phys. Rev. Lett. **109**, 263004 (2012).

[56] T. Nicholson, S. Campbell, R. Hutson, G. Marti, B. Bloom, R. McNally, W. Zhang, M. Barrett, M. Safronova, W. Strouse, G. F. Tew, and J. Ye, Nat. Commun. **6**, 6896 (2015).

[57] M. Naftaly and R. E. Miles, Proc. IEEE **95**, 1658 (2007).

[58] T. Middelmann, C. Lisdat, S. Falke, J. S. R. Vellore Winfred, F. Riehle, and U. Sterr, IEEE Trans. Instrum. Meas. **60**, 2550 (2011).

[59] R. Le Targat, L. Lorini, Y. Le Coq, M. Zawada, J. Guéna, M. Abgrall, M. Gurov, P. Rosenbusch, D. G. Rovera, B. Nagórny, R. Gartman, P. Westergaard, M. Tobar, M. Lours, G. Santarelli,

A. Clairon, S. Bize, P. Laurent, P. Lemonde, and J. Lodewyck, Nat. Commun. **4**, 2109 (2013).

[60] N. D. Lemke, J. von Stecher, J. A. Sherman, A. M. Rey, C. W. Oates, and A. D. Ludlow, Phys. Rev. Lett. **107**, 103902 (2011).

[61] T. Zelevinsky, M. M. Boyd, A. D. Ludlow, T. Ido, J. Ye, R. Ciuryło, P. Naidon, and P. S. Julienne, Phys. Rev. Lett. **96**, 203201 (2006).

[62] K. Gibble, Phys. Rev. Lett. **110**, 180802 (2013).

[63] J. Mitroy and J. Zhang, Mol. Phys. **108**, 1999 (2010).

[64] P. Lemonde and P. Wolf, Phys. Rev. A **72**, 033409 (2005).

[65] T. Akatsuka, M. Takamoto, and H. Katori, Nat. Phys. **4**, 954 (2008).

[66] C. Radzewicz, M. Bober, P. Morzyński, A. Cygan, D. Lisak, D. Bartoszek-Bober, P. Masłowski, P. Ablewski, J. Zachorowski, W. C. R. Gawlik, and M. Zawada, Phys. Scr. **91**, 084003 (2016).

[67] Using the ^{87}Sr frequency value from Comité International des Poids et Mesures, 98th Meeting (October 2009); Recommendation 2 (CI-2009), p. 235.

[68] V. I. Yudin, A. V. Taichenachev, C. W. Oates, Z. W. Barber, N. D. Lemke, A. D. Ludlow, U. Sterr, C. Lisdat, and F. Riehle, Phys. Rev. A **82**, 011804(R) (2010).

[69] C. Sanner, N. Huntemann, R. Lange, C. Tamm, and E. Peik, Phys. Rev. Lett. **120**, 053602 (2018).

[70] S. Origlia, private communication.

[71] M. M. Boyd, T. Zelevinsky, A. D. Ludlow, S. Blatt, T. Zanon-Willette, S. M. Foreman, and J. Ye, Phys. Rev. A **76**, 022510 (2007).